

Current switching behaviour mediated via hinge modes in higher order topological phase using altermagnets

Minakshi Subhadarshini , ^{1, 2, *} Amartya Pal , ^{1, 2, *} and Arijit Saha , ^{1, 2, †}

¹ Institute of Physics, Sachivalaya Marg, Bhubaneswar-751005, India

² Homi Bhabha National Institute, Training School Complex, Anushakti Nagar, Mumbai 400094, India

We propose a theoretical framework to engineer hybrid-order and higher-order topological phases in three-dimensional topological insulators by coupling to d -wave altermagnets (AMs). Presence of only $d_{x^2-y^2}$ -type AM drives the system into a hybrid-order topological phase where both first-order and second-order topological phases coexist. This phase is characterized by spectral analysis, low-energy surface theory, dipolar and quadrupolar winding numbers, and its signature is further confirmed by two-terminal differential conductance calculations. Incorporation of the $d_{x^2-z^2}$ -type AM drives the system into two second-order topological insulator phases hosting distinct type of hinge modes. They are also topologically characterized by spectral analysis, topological invariants, low-energy surface theory, and transport calculations. Importantly, the localization and direction of propagation of these one-dimensional hinge modes are controllable by tuning the relative strengths of the alermagnetic exchange orders. We utilize this feature to propose a tunable current-switching behaviour mediated via the hinge modes. Our results establish AMs based hybrid structure as a versatile platform for controllable higher-order topology and hinge-mediated device applications.

Introduction:— The advent of altermagnets (AMs) [1–4] has led to a surge of research activity in the condensed matter community. AMs represent a class of antiferromagnets with centro-symmetric collinear-compensated magnetic order. Unlike conventional ferromagnets, which exhibit uniform magnetization and spin-split energy bands, and unlike antiferromagnets with zero magnetization and no spin-splitting of energy bands, AMs feature both zero magnetization and momentum-dependent spin-split electronic bands. Furthermore, AMs break the combined parity (\mathcal{P}) and time-reversal symmetry (\mathcal{T}) giving rise to such momentum-dependent spin-splitting of energy bands i.e., $E(\sigma, \mathbf{k}) \neq E(-\sigma, \mathbf{k})$. In d -wave AMs, opposite spin-sublattices are mapped onto each other by a C_{4z} rotation rather than translation or reflection, which exhibits the net magnetization zero. Interestingly, d -wave AMs can be considered as a Zeeman field where the momentum-dependent magnetic order resembles the shape of the atomic planar d -orbitals instead of being uniform. This unique unconventional magnetic phase gives rise to a plethora of theoretical works e.g., anomalous Hall effect [5–8], anisotropic spin-polarized conductivity [9], anisotropic magnetoresistance [10], efficient spin-charge conversion [11, 12], topological superconductivity [13–18], Josephson effect [19–22] etc. Various candidate materials with such anisotropic spin-polarized Fermi surfaces are proposed such as RuO_2 [12, 23], MnF_2 [4], MnTe [3] etc.

In recent times, the concept of higher-order topology generalizes the conventional bulk-boundary correspondence to boundaries of reduced dimensionality. While first-order topological insulators (TIs) host gapless states on $(d-1)$ -dimensional surfaces [24], an n^{th} -order topo-

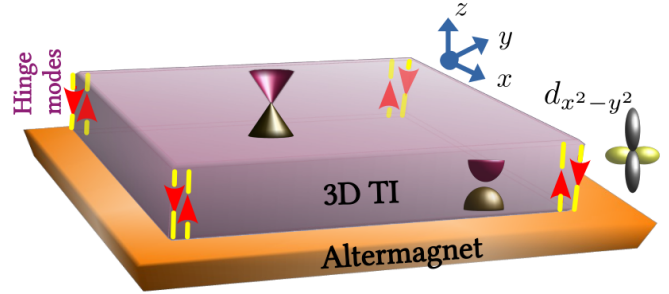


FIG. 1. **Schematic diagram of our setup:** Schematic illustration of a 3D first-order topological insulator (purple, top) placed on the surface of a d -wave AM (orange, bottom) with both $(x^2 - y^2)$ and $(x^2 - z^2)$ (not shown) symmetry components. The 1D hinge states are shown by the yellow lines propagating along $\pm z$ directions (marked by the red arrows). The top surface hosts gapless Dirac cones, while the front surface is gapped.

logical insulator supports modes localized on $(d-n)$ -dimensional boundaries, such as hinges or corners [25–32]. These higher-order topological phases (HOTPs) ($n > 1$) can arise from crystalline symmetries including reflection, rotation, and inversion [33–35], and have been realized in diverse material platforms such as metamaterials [36, 37], bismuth-based compounds and transition-metal dichalcogenides [38–40] etc. Also, HOTPs utilizing the d -wave AMs have been recently theoretically investigated in two dimensions (2D) [41–45].

Very recently, the idea of higher-order topology has been extended to hybrid-order topological phases (HyOTPs) that embody both first-order and second-order topological phases e.g., higher-order Weyl semimetals [46, 47], higher-order nodal line semimetals [48–51] etc. However, a systematic generation of HOTPs and HyOTPs based on alermagnetic platforms in 3D has not been investigated so far, to the best of our knowledge.

* MS and AP contributed equally to this work.

† arijit@iopb.res.in

Moreover, the exchange order in d -wave AMs closely mimics the Wilson-Dirac (WD) mass term, essential for realizing HOTPs [38, 52]. However, WD mass preserves the combined \mathcal{PT} symmetry, whereas AMs break \mathcal{PT} -symmetry. Thus, it would be really interesting to investigate the role of AMs in realizing HOTPs and HyOTPs in 3D. Given this background, in this article, we ask the following intriguing questions: (i) Can altermagnetic exchange generate both HOTPs and HyOTPs in 3D? (ii) If HyOTP and HOTP emerge, then how can they be distinctly identified in transport calculation? and (iii) Can higher-order boundary modes (1D hinge modes) be manipulated to yield an elegant, device-relevant transport functionality?

To address these interesting questions, we propose a theoretical model consisting of d -wave AMs with $d_{x^2-y^2}$ and $d_{x^2-z^2}$ symmetry and a 3D TI as schematically shown in Fig. S1. Our analysis identifies two distinct classes of topological phases: (i) a HyOTP with coexisting 2D surface and 1D hinge modes, (see Fig. S2) and (ii) a purely second-order topological insulator (SOTI) phase hosting only 1D hinge-localized modes (see Fig. 4). In addition to topological invariants such as dipolar winding number (DWN), quadrupolar winding number (QWN), and spectral analysis, we also identify the HyOTP using transport calculation (see Fig. 3). We also derive the effective low-energy surface theory to analytically understand the role of AMs order. Importantly, we find the emergence of two types of SOTI phases where the localization and direction of propagation of hinge modes are controllable by the relative strengths of AMs. Utilizing this feature, we propose a current-switching like behaviour, where the conducting properties of the system can be controlled by tuning the strength of the AMs, which are consistent with both analytical predictions and numerical simulations.

Model:— To begin with, we consider our system to be composed of a 3D first order TI placed on top of 2D d -wave AMs as schematically illustrated in Fig. S1. This can be described by the following tight-binding Hamiltonian in the momentum space on a cubic lattice as [2, 53, 54],

$$\mathcal{H}(\mathbf{k}) = \mathcal{H}^{\text{TI}}(\mathbf{k}) + \mathcal{H}_{xy}^{\text{AM}}(\mathbf{k}) + \mathcal{H}_{xz}^{\text{AM}}(\mathbf{k}) , \quad (1)$$

with,

$$\begin{aligned} \mathcal{H}^{\text{TI}}(\mathbf{k}) &= 2\lambda(\sin k_x \Gamma_1 + \sin k_y \Gamma_2 + \sin k_z \Gamma_3) \\ &+ [m_0 - 6t + 2t \sum_{i=x,y,z} \cos k_i] \Gamma_4 , \end{aligned} \quad (2)$$

$$\mathcal{H}_{xy}^{\text{AM}}(\mathbf{k}) = J_{xy}(\cos k_x - \cos k_y) \Gamma_5 , \quad (3)$$

$$\mathcal{H}_{xz}^{\text{AM}}(\mathbf{k}) = J_{xz}(\cos k_z - \cos k_x) \Gamma_5 . \quad (4)$$

where, \mathcal{H}^{TI} , $\mathcal{H}_{xy}^{\text{AM}}$, and $\mathcal{H}_{xz}^{\text{AM}}$ represent the 3D TI, d -wave AMs having $d_{x^2-y^2}$, and $d_{x^2-z^2}$ symmetry, respectively. The model parameters λ , t , and m_0 denote the strength

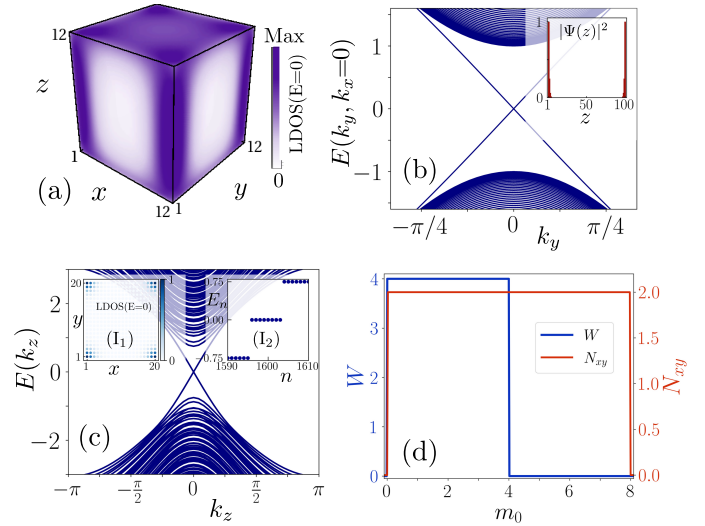


FIG. 2. Spectral properties and topological invariants in the HyOTP: In panel (a), we show the LDOS ($E = 0$) in the HyOTP considering a finite geometry along the x , y , and z directions with $L_x = L_y = L_z = 12$ lattice sites. Panel (b) displays the energy spectrum, corresponding to finite system size along z directions with $L_z = 100$, as a function of k_y with $k_x = 0$, while the inset exhibits the spatial profile $|\psi(z)|^2$ at $k_x = k_y = 0$. Panel (c) shows the hinge spectrum as a function of k_z , with insets (I_1, I_2) illustrating the LDOS at $E = 0$ and the eigenvalue spectrum with respect to eigenstate index n with $L_x = L_y = 20$. In panel (d), we present the topological invariants, DWN W (left axis) and QWN N_{xy} (right axis) as a function of m_0 . Other model parameters are chosen as, $m_0 = t$, $t = 1$, $\lambda = t$, and $J_{xy} = 2t$.

of the intrinsic spin-orbit coupling (SOC), nearest neighbour hopping amplitude, and staggered mass term originating from crystal field splitting [24]. The altermagnetic exchange order is assumed to be induced in the bulk of 3D TI via the proximity effect. Here, J_{xy} , J_{xz} represent the strength of the altermagnetic exchange terms with $d_{x^2-y^2}$ and $d_{x^2-z^2}$ symmetry, respectively. The (8×8) Γ matrices are chosen to form a set of anti-commuting matrices and defined as, $\Gamma_1 = \mu_x \sigma_x s_y$, $\Gamma_2 = \mu_z \sigma_0 s_0$, $\Gamma_3 = \mu_x \sigma_z s_y$, $\Gamma_4 = \mu_x \sigma_0 s_y$, $\Gamma_5 = \mu_x \sigma_0 s_z$ where, μ_i , σ_i , and s_i ($i = 0, x, y, z$) are Pauli matrices operating in the sublattice, orbital, and spin degrees of freedom.

The Hamiltonian for the 3D TI, $\mathcal{H}^{\text{TI}}(\mathbf{k})$ (Eq. (2)) represents a first-order TI with gapless Dirac like surface states for $0 < m_0 < 4t$ [24]. Also, $\mathcal{H}^{\text{TI}}(\mathbf{k})$ respects the TRS of the system with $\mathcal{T} = i\mu_x \sigma_0 s_y \mathcal{K}$, \mathcal{K} being the complex-conjugation operator: $\mathcal{T}^{-1} \mathcal{H}^{\text{TI}}(\mathbf{k}) \mathcal{T} = \mathcal{H}^{\text{TI}}(-\mathbf{k})$. We refer the readers to supplementary material (SM) [55] for further details on band structure and spatial distribution of the surface states. The altermagnetic Hamiltonians $\mathcal{H}_{xy}^{\text{AM}}(\mathbf{k})$ and $\mathcal{H}_{xz}^{\text{AM}}(\mathbf{k})$ individually break the TRS of the system and gaps out the surface states. However, in principle, one can also consider AMs with d_{xy} (d_{xz}) symmetry which can be mapped into the $d_{x^2-y^2}$ ($d_{x^2-z^2}$)-symmetry by rotating the coordinate axis via an angle of $\pi/4$ (see

SM [55] for details). Nevertheless, we consider AMs with only $d_{x^2-y^2}$ and $d_{x^2-z^2}$ -symmetry for simplicity.

Emergence of hybrid-order topology and its topological characterization:— We first discuss the effect of only $\mathcal{H}_{xy}^{\text{AM}}(\mathbf{k})$ on the surface states of 3D TI. We systematically study the spectral features like band structure, local density of states (LDOS) to probe the bulk-boundary correspondence, and topological invariants to characterize the HyOTP. First, we compute the site-resolved LDOS of the zero-energy eigenstates of $\mathcal{H}(\mathbf{k})$ by diagonalizing the Hamiltonian in real space with a finite system size L_x, L_y , and L_z along the x, y , and z directions employing open boundary conditions (OBC). The corresponding LDOS ($E = 0$) is depicted in the Fig. S2(a) which indicates the presence of both surface- and hinge-localized boundary states. The surface states appear in the $x - y$ plane ($z = 0, L_z$) while the hinge modes appear perpendicular to the $x - y$ plane i.e., along z -direction. To identify these surface states, we diagonalize $\mathcal{H}(\mathbf{k})$ in slab geometry (see SM [55] for details) and display the band structure in Fig. S2(b) as a function of k_y with $k_x = 0$. This exhibits the presence of gapless states. From the LDOS ($E = 0$) behavior (inset of Fig. S2(b)) we find the gapless states to be localized around $z = 0$ and $z = L_z$, confirming them to be surface states.

Then, in order to identify the hinge localized modes, we compute the energy-eigenvalues of the Hamiltonian $\mathcal{H}(\mathbf{k})$ considering rod geometry (see SM [55] for details) and depict as a function of k_z in the Fig. S2(c). We observe the emergence of gapless dispersive states, crossing each other at $k_z = 0$. Furthermore, we calculate the energy eigenvalues, E_n , and LDOS ($E = 0$) by setting $k_z = 0$. We depict the variation of E_n as a function of state index, n , in the inset (I_1) and the LDOS ($E = 0$) in the inset (I_2) of Fig. S2(c) respectively. From these plots, we infer the appearance of a total of eight gapless hinge-localized states establishing the emergence of SOTI in 3D.

To this end, we topologically characterize the HyOTP by computing the DWN W , and QWN N_{xy} to identify the first and second order topological phases, respectively. The DWN, used to characterize a gapped 1D topological phase is defined as [17, 51, 56],

$$W = \frac{i}{2\pi} \int_{\text{BZ}} dk_z \text{Tr}[h^{-1}(k_z) \partial_{k_z} h(k_z)] , \quad (5)$$

where, $h(k)$ can be obtained by antidiagonalizing $\mathcal{H}(\mathbf{k})$ of Eq. (S3) in the chiral basis with chiral operator $\mathcal{S} = \mu_0 \sigma_x s_0$. We obtain an effective 1D system by setting $k_x = k_y = 0$ in $\mathcal{H}(\mathbf{k})$ since the surface states intersect with each other at $k_x = k_y = 0$ (see Fig. S2(b)). We refer the readers to SM [55] for further details.

On the other hand, QWN is utilized to characterize the SOTIs in 2D, which we obtain by setting $k_z = 0$ in $\mathcal{H}(\mathbf{k})$ since the hinge modes intersect at $k_z = 0$. Exploiting the chiral symmetry ($\mathcal{S} = \mu_y \sigma_z s_z$) in this geometry, the QWN can be defined as as [51, 57, 58],

$$N_{xy} = \frac{1}{2\pi i} \text{Tr} \ln \left(\bar{Q}_A \bar{Q}_B^\dagger \right) , \quad (6)$$

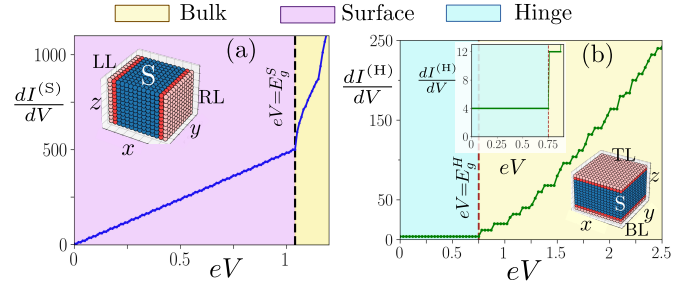


FIG. 3. Transport characteristics in the HyOTP: In panel (a), we depict the differential conductance $\frac{dI^{(\text{S})}}{dV}$ as a function of (eV) , due to the surface states in HyOTP. The inset illustrates the transport setup with LL (left lead), RL (right lead), and S (system) through which the current flows. Panel (b) presents the differential conductance $\frac{dI^{(\text{H})}}{dV}$ with respect to (eV) for the hinge states. The inset (bottom) highlights the transport setup with top and bottom leads (TL and BL). On the other hand, the inset (top) emphasizes the $4e^2/h$ contribution arising due to hinge modes of the main plot. For panel (a) $L_z = 100$ and panel (b) $L_x = L_y = 20$. Other model parameters remain same as mentioned in Fig. S2.

where, $\bar{Q}_{A,B}$ stands for sublattice quadrupole operator, defined as $\bar{Q}_{A,B} = U_{A,B}^\dagger U_{A,B}^S Q U_{A,B}^S U_{A,B}^\dagger$ with the quadrupole operator given by, $Q = \exp(-2\pi i xy/L_x L_y)$. The $U_{A(B)}^S$ and $U_{A(B)}$ are unitary matrices obtained from the chiral symmetry operator and anti-diagonalizing the $\mathcal{H}(\mathbf{k})$ (see SM [55] for further details).

We discuss the variation of W (left axis) and N_{xy} (right axis) as a function of the staggered mass term m_0 in Fig. S2(d). For $0 \leq m_0 \leq 4t$, W is nonzero while zero outside this range, which still corresponds to the topological regime of the parent 3D TI [24]. In contrast, $N_{xy} = 2$ for $0 \leq m_0 \leq 8t$, which indicates the presence of SOTI phase with two modes per hinge and validates our results as shown in Fig. S2(c). Thus, for $0 < m_0 < 4t$, both W and N_{xy} are nonzero which confirm the presence of HyOTP comprised of both first and second order topological phases. Importantly, outside the topological regimes of the 3D TI i.e., $4t \leq m_0 \leq 8t$, $N_{xy} = 2$ and $W = 0$, leading to the emergence of a pure SOTI phase. Therefore, the presence of AM also extends the topological phase boundary beyond that of the first-order 3D TI.

For a more fundamental understanding of the role of AM in realizing the HyOTP, we analytically derive the low-energy effective Hamiltonians for xy , yz , and xz surfaces utilizing the low-energy surface theory as, [52, 58] (for details see SM [55]):

$$H_{xy}^S = -2\lambda k_x \sigma_x s_y - 2\lambda k_y \sigma_z s_0 , \quad (7)$$

$$H_{yz}^S = -2\lambda k_y \sigma_z s_0 + 2\lambda k_z \sigma_x s_y + \frac{J_{xy} m_0}{2t} \sigma_x s_z , \quad (8)$$

$$H_{xz}^S = -2\lambda k_x \sigma_z s_0 + 2\lambda k_z \sigma_x s_0 + \frac{J_{xy} m_0}{2t} \sigma_y s_x . \quad (9)$$

From these effective Hamiltonians, it is evident that xy -surface states do not acquire any mass term, reflecting

the gapless surface state as the signature of first-order topology, while the yz and xz surfaces become gapped due to the acquired mass terms ($\propto J_{xy}m_0$). To compare the induced mass terms in the yz and xz surface, we perform a unitary transformation in H_{xz} and show that xz - and yz -surfaces acquire equal and opposite masses, $\pm(J_{xy}m_0/2t)$ (see SM [55] for details). This creates a mass-domain wall configuration. Such a domain wall configuration supports zero-energy Jackiw-Reby modes which reflect as hinge modes in the SOTI phase in 3D system [59].

Transport characteristics of the HyOTP:— After discussing the spectral features in details, we now focus on the transport properties of the HyOTP. In particular, we compute the two-terminal differential conductance (dI/dV) within the Landauer-Buttiker formalism [60] utilizing the Python package Kwant [61]. The gapless Dirac surface states, located at $z = 0$ and $z = L_z$, disperse linearly with momentum along x - and y -directions (see Eq.(7)). Thus, without loss of generality, we attach two semi-infinite leads at $x = 0$ (left lead (LL)) and $x = L_x$ (right lead (RL)) as shown in the inset of Fig.3(a). We compute the differential conductance dI/dV in this geometry in the presence of a voltage bias, eV , at zero temperature as, [51, 60–62],

$$\frac{dI^{(S)}}{dV}(eV) = \frac{e^2}{h} \sum_{k_y} \text{Tr} \left[t_S^\dagger(E) t_S(E) \right]_{E=eV}, \quad (10)$$

Here, $t_S(E)$ denotes the transmission amplitude matrix for the geometry under consideration. The summation \sum_{k_y} takes into account the propagating modes along the y -direction (see SM [55] for the details).

To identify the dispersive hinge modes propagating along the $\pm z$ direction (as illustrated in Fig.S2(c)), we compute the differential conductance by attaching two leads at $z = 0$ (bottom lead (BL)) and $z = L_z$ (top lead, (TL)) with a finite size system L_x and L_y along x and y directions as shown in the inset of Fig.3(b). The differential conductance in this geometry can be obtained as [51, 60–62],

$$\frac{dI^{(H)}}{dV}(eV) = \frac{e^2}{h} \text{Tr} \left[t_H^\dagger(E) t_H(E) \right]_{E=eV}, \quad (11)$$

where, the transmission matrix ‘ $t_H(E)$ ’ incorporates all the information about the transverse modes (see SM [55] for details). Note that, the leads are considered to be of the same material as the system for simplicity.

We showcase the behavior of $\frac{dI}{dV}^{(S)}(eV)$ and $\frac{dI}{dV}^{(H)}(eV)$ (in units of e^2/h) as a function of eV in Fig.3(a) and Fig.3(b), respectively. In Fig.3(a), $\frac{dI}{dV}^{(S)}$ initially grows linearly with eV within the bulk gap $E = E_g^S$. The reason can be attributed to the fact that the gapless Dirac surface states exist only within the bulk gap and disperse linearly with momentum k_x, k_y around the Dirac point. This leads to linearly varying density of states in 2D i.e., $\text{DOS}(E) \sim E$ for $E \leq E_g^S$, which is being

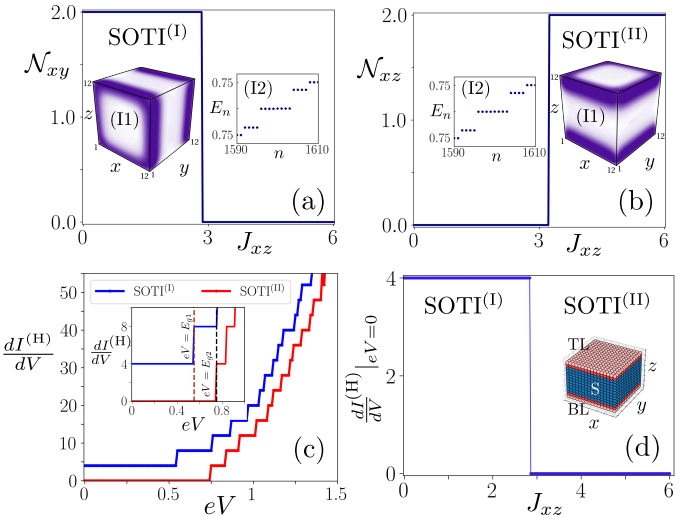


FIG. 4. **Topological characterization and current switching behavior in the SOTI phase.** We depict N_{xy} and N_{xz} for the xy - and xz -planes in panels (a) and (b), corresponding to SOTI^(I) and SOTI^(II) phases respectively. Insets (I1) and (I2) illustrate the eigenvalue spectrum E_n with respect to n . The LDOS distribution at $E = 0$ for both the cases are also shown in panels (a) and (b). Panel (c): $dI^{(H)}/dV$ is displayed as a function of bias eV for the SOTI^(I) ($J_{xz} = 2t$) and SOTI^(II) phase ($J_{xz} = 4t$); the inset exhibits an expanded view of the same conductance plot to highlight the contribution arising from the hinge modes. (d) $dI^{(H)}/dV(eV = 0)$ is illustrated as a function of J_{xz} , with the corresponding transport device setup given in the inset. The other model parameters are chosen as, $m_0 = t$, $t = 1$, $\lambda = t$, $J_{xy} = 3t$ and $L_x = L_y = 20$.

reflected in the transport calculation as a linear dependency with eV . For $E > E_g^S$, $\frac{dI}{dV}^{(S)}$ deviates from the linear variation as it encounters the density of states due to the bands of the Dirac cone, which is not linear in E .

In case of $\frac{dI}{dV}^{(H)}(eV)$, we obtain a quantized conductance of $4e^2/h$ for $eV \leq E_g^H$ as depicted in Fig.3(b) and its inset for better clarity. This quantization arises because the system hosts eight hinge modes in total, four propagating along $+z$ and four along $-z$ direction. Since the voltage bias eV is applied across the top and bottom lead (TL and BL), $\frac{dI}{dV}^{(H)}$ captures the signature of hinge modes propagating only along the $-z$ direction, leading to quantized conductance of $4e^2/h$. While such quantization is absent for the bulk states, $E > E_g^H$ and $\frac{dI}{dV}^{(H)}$ becomes continuous. These results confirm that the HyOTP contains both surface and hinge-localized modes, as clearly demonstrated in the transport signatures.

Emergence of SOTI and its implications in current-switching behavior via hinge modes:— We here incorporate the AM with $d_{x^2-z^2}$ -symmetry and systematically analyse the spectral and transport properties. We establish the emergence of two types of SOTI phase with 1D hinge modes. Interestingly, the localization and direction

of propagation of these hinge modes can be controlled by tuning the strength of J_{xz} relative to J_{xy} . We first derive the low energy-effective Hamiltonian in case of both $J_{xy}, J_{xz} \neq 0$, and obtain the induced mass terms on each surface with the following dependency on J_{xy} and J_{xz} as, xy -surface: $\frac{J_{xz}m_0}{2t}$, yz -surface: $\frac{(J_{xy} - J_{xz})m_0}{2t}$, and xz -surface: $-\frac{J_{xy}m_0}{2t}$ (see SM [55] for details). Interestingly, the xy surface now acquires a finite mass gap due to finite J_{xz} . However, the sign of mass term on the yz surface depends on the relative strength of J_{xy} and J_{xz} , which leads to the emergence of two types of SOTI phases, (i) SOTI^(I) for $J_{xz} < J_{xy}$ (see LDOS (E=0) plot in the inset of Fig. 4(a)), and (ii) SOTI^(II) for $J_{xz} > J_{xy}$ (see LDOS (E=0) behavior in the inset of Fig. 4(b)). Note that, SOTI^(I) phase consists of eight hinge modes propagating along the x and z directions, while SOTI^(II) phase anchors eight hinge modes propagating along the x and y directions. We topologically characterize the SOTI^(I) and SOTI^(II) phases by computing QWNs N_{xy} and N_{xz} , respectively. The QWN N_{xz} is computed similarly as N_{xy} (as outlined in Eq. (6)) with chiral symmetry $\mathcal{S} = \mu_0\sigma_0s_x$ (see SM [55] for further details). In particular, N_{xy} (N_{xz}) characterize the hinge modes which are localized in the xy (xz) plane and propagate along the z (y) direction. We depict the variation of N_{xy} and N_{xz} by varying the strength of J_{xz} with fixed $J_{xy} = 3t$ in Fig. 4(a) and Fig. 4(b), respectively. We find that $(N_{xy}, N_{xz}) = (2, 0)$ for $J_{xz} < J_{xy}$ which corresponds to the SOTI^(I) phase. On the other hand, $(N_{xy}, N_{xz}) = (0, 2)$ for $J_{xz} > J_{xy}$ corresponds to the SOTI^(II) phase.

To identify the two types of SOTI phases in transport, we consider a setup where two leads are attached at $z = 0$ (BL) and at $z = L_z$ (TL) (see the inset of Fig. 4(d) for the setup), with a finite size system along the x and y directions. A voltage bias, eV , is applied across the top and bottom leads to compute the differential conductance resulting from the hinge modes propagating along the z -direction. We compute and depict the corresponding $\frac{dI}{dV}(eV)$ (Eq. (11)) in Fig. 4(c) in case of both the SOTI^(I) and SOTI^(II) phases. Moreover, in the inset of Fig. 4(c), we mark the bulk gaps, E_{g1} (in the SOTI^(I) phase) and E_{g2} (in case of SOTI^(II) phase) to explicitly highlight the contribution to the conductance arising from the hinge states ($eV < E_{g1}, E_{g2}$) and bulk states ($eV > E_{g1}, E_{g2}$). Interestingly, we observe that $\frac{dI}{dV}$ attains a quantized value of $4e^2/h$ for $E \leq E_{g1}$ only in the SOTI^(I) phase, while $\frac{dI}{dV}$ remains zero for $eV \leq E_{g2}$ in case of SOTI^(II) phase. The reason can be attributed to the fact that in the SOTI^(I) phase, four gapless dispersive hinge modes are propagating along the z -direction, which results in a total conductance of $4e^2/h$. However, such hinge modes are absent in the SOTI^(II) phase. We then compute the zero-bias conductance, $\frac{dI}{dV}|_{eV=0}$, by varying the strength of J_{xy}

and present the results in Fig. 4(d). Notably, we observe that $\frac{dI}{dV}|_{eV=0}$ becomes non-zero and quantized when $J_{xz} < J_{xy}$ while it is zero if $J_{xz} > J_{xy}$. This is due to the fact that the gapless hinge modes propagating along the z -direction exist only in the SOTI^(I) phase i.e., for $J_{xz} < J_{xy}$ (see Fig. 4(a)), which leads to the conductance quantization. Whereas, for $J_{xz} > J_{xy}$, the system enters into the SOTI^(II) phase where hinge modes propagate only along the x and y direction, not along the z -direction (see Fig. 4(b)). This special feature can be utilized as a current-switching mechanism mediated via the 1D hinge modes where, tuning the strength of J_{xz} relative to J_{xy} , one can control the direction of current flow along a particular direction. However, by choosing appropriate lead configuration, one can also make SOTI^(II) phase conducting in this switching behavior. This feature might carry high relevance and utility in modern electronic devices.

Summary and Conclusion:— To summarize, in this article, we put forward a theoretical framework for realizing both HOTPs and HyOTPs in a 3D TI proximitized with d -wave AMs with $d_{x^2-y^2}$ and $d_{x^2-z^2}$ symmetries. Coupling only to the $d_{x^2-y^2}$ AM drives the system into a HyOTP with gapless 2D Dirac surface states (first order) coexisting with the 1D hinge-localized modes (second order). Through a systematic analysis of spectral properties together with dipolar and quadrupolar winding numbers, we establish the existence of this HyOTP. Employing a low-energy surface theory, we analytically derive the effective Hamiltonians for each surface, clarifying how the AM exchange fields gap out selected surface states resulting in appearance of hinge modes. Finally, computing differential conductance within the Landauer-Buttiker formalism [60], we identify both surface and hinge transport channels, providing clear signatures of the hybrid-order topology.

In presence of both $d_{x^2-y^2}$ and $d_{x^2-z^2}$ AMs the system hosts two distinct SOTI phases, SOTI^(I) and SOTI^(II) where the localization and direction of propagation of the hinge modes are controlled solely by the relative strengths of the two AM components. Utilizing this feature, we demonstrate a hinge-mediated current-switching mechanism. For a given transport setup, SOTI^(I) phase exhibits nonzero quantized $dI^{(H)}/dV(eV = 0)$, whereas SOTI^(II) phase do not conduct. Thus, by simply tuning the AM exchange strengths, one can control the hinge-mode transport, effectively realizing a topological current switch with possible potential device relevance. As possible materials, one may use the heterostructure of Bi_2Se_3 - RuO_2 [12, 23, 53].

So far, our discussion has centered around how the interplay between a first order 3D TI and 2D d -wave AMs gives rise to second-order topological phase in 3D. We now propose an additional route to realize a third-order TI (TOTI) phase in 3D by introducing an unconventional magnetic order that mimics the spatial profile of a d_{z^2} orbital, $\mathcal{H}_{d_{z^2}}(\mathbf{k}) \sim 2\cos k_z - \cos k_x - \cos k_y$. In the SM [55], we present a detailed analysis of this TOTI phase, including band structure, LDOS, topological invariant, and an

analytic derivation of the effective hinge Hamiltonians supporting the numerical findings. We emphasize that such a d_{z^2} -type magnetic order is purely theoretical and currently lacks any material realization reported in literature. As a possible future direction, one may also explore the influence of d_{xy} - or d_{xz} -type AMs and combination of both $d_{x^2-y^2}$ and d_{xy} -type AMs in further manipulating HOTPs.

Acknowledgments:— We acknowledge the Department

of Atomic Energy (DAE), Govt. of India for providing the financial support. We also acknowledge SAMKHYA: High-Performance Computing Facility provided by Institute of Physics, Bhubaneswar and the two workstations provided by the Institute of Physics, Bhubaneswar from the DAE APEX project for numerical computations.

Data Availability Statement:— The datasets generated and analyzed during the current study are available from the corresponding author upon reasonable request.

[1] L. Šmejkal, J. Sinova, and T. Jungwirth, “*Emerging Research Landscape of Altermagnetism*,” *Phys. Rev. X* **12**, 040501 (2022).

[2] L. Šmejkal, J. Sinova, and T. Jungwirth, “*Beyond Conventional Ferromagnetism and Antiferromagnetism: A Phase with Nonrelativistic Spin and Crystal Rotation Symmetry*,” *Phys. Rev. X* **12**, 031042 (2022).

[3] I. I. Mazin, “*Altermagnetism in MnTe: Origin, predicted manifestations, and routes to detwinning*,” *Phys. Rev. B* **107**, L100418 (2023).

[4] S. Bhowal and N. A. Spaldin, “*Ferroically Ordered Magnetic Octupoles in d-Wave Altermagnets*,” *Phys. Rev. X* **14**, 011019 (2024).

[5] T. Sato, S. Haddad, I. C. Fulga, F. F. Assaad, and J. van den Brink, “*Altermagnetic Anomalous Hall Effect Emerging from Electronic Correlations*,” *Phys. Rev. Lett.* **133**, 086503 (2024).

[6] V. A. Zyuzin, “*Metallic collinear antiferromagnets with mirror-symmetric and asymmetric spin splittings*,” *Phys. Rev. B* **112**, 165104 (2025).

[7] S. Sorn and Y. Mokrousov, “*Activation of anomalous Hall effect and orbital magnetization by domain walls in altermagnets*,” *Phys. Rev. B* , (2025).

[8] L. Attias, A. Levchenko, and M. Khodas, “*Intrinsic anomalous Hall effect in altermagnets*,” *Phys. Rev. B* **110**, 094425 (2024).

[9] M. Dou, X. Wang, and L. L. Tao, “*Anisotropic spin-polarized conductivity in collinear altermagnets*,” *Phys. Rev. B* **111**, 224423 (2025).

[10] R. D. G. Betancourt, J. Zubáč, K. Geishendorf, P. Ritzinger, B. Růžičková, T. Kotte, J. Železný, K. Olejník, G. Springholz, B. Büchner, A. Thomas, K. Výborný, T. Jungwirth, H. Reichlová, and D. Kriegner, “*Anisotropic magnetoresistance in altermagnetic MnTe*,” *npj Spintronics* **2**, 45 (2024).

[11] M. Leiviskä, J. Rial, A. Bad'ura, R. L. Seeger, I. Kounta, S. Beckert, D. Kriegner, I. Journaud, E. Schmoranzerová, J. Sinova, O. Gomonay, A. Thomas, S. T. B. Goennenwein, H. Reichlová, L. Šmejkal, L. Michez, T. c. v. Jungwirth, and V. Baltz, “*Anisotropy of the anomalous Hall effect in thin films of the altermagnet candidate Mn₅Si₃*,” *Phys. Rev. B* **109**, 224430 (2024).

[12] H. Bai, Y. C. Zhang, Y. J. Zhou, P. Chen, C. H. Wan, L. Han, W. X. Zhu, S. X. Liang, Y. C. Su, X. F. Han, F. Pan, and C. Song, “*Efficient Spin-to-Charge Conversion via Altermagnetic Spin Splitting Effect in Antiferromagnet RuO₂*,” *Phys. Rev. Lett.* **130**, 216701 (2023).

[13] S. A. A. Ghorashi, T. L. Hughes, and J. Cano, “*Altermagnetic Routes to Majorana Modes in Zero Net Magnetization*,” *Phys. Rev. Lett.* **133**, 106601 (2024).

[14] Y.-X. Li, “*Realizing tunable higher-order topological superconductors with altermagnets*,” *Phys. Rev. B* **109**, 224502 (2024).

[15] D. Zhu, Z.-Y. Zhuang, Z. Wu, and Z. Yan, “*Topological superconductivity in two-dimensional altermagnetic metals*,” *Phys. Rev. B* **108**, 184505 (2023).

[16] K. Maeda, Y. Fukaya, K. Yada, B. Lu, Y. Tanaka, and J. Cayao, “*Classification of pair symmetries in superconductors with unconventional magnetism*,” *Phys. Rev. B* **111**, 144508 (2025).

[17] D. Mondal, A. Pal, A. Saha, and T. Nag, “*Distinguishing between topological Majorana and trivial zero modes via transport and shot noise study in an altermagnet heterostructure*,” *Phys. Rev. B* **111**, L121401 (2025).

[18] O. Alam, A. Pal, P. Dutta, and A. Saha, “*Proximity-induced superconductivity and emerging topological phases in altermagnet-based heterostructures*,” *arXiv:2510.26894 [cond-mat.supr-con]*.

[19] J. A. Ouassou, A. Brataas, and J. Linder, “*dc Josephson Effect in Altermagnets*,” *Phys. Rev. Lett.* **131**, 076003 (2023).

[20] B. Lu, K. Maeda, H. Ito, K. Yada, and Y. Tanaka, “ *φ Josephson Junction Induced by Altermagnetism*,” *Phys. Rev. Lett.* **133**, 226002 (2024).

[21] L. Sharma and M. Thakurathi, “*Tunable Josephson diode effect in singlet superconductor-altermagnet-triplet superconductor junctions*,” *Phys. Rev. B* **112**, 104506 (2025).

[22] A. Pal, D. Mondal, T. Nag, and A. Saha, “*Josephson current signature of Floquet Majorana and topological accidental zero modes in altermagnet heterostructures*,” *Phys. Rev. B* **112**, L201408 (2025).

[23] D. T. Plouff, L. Scheuer, S. Shrestha, W. Wu, N. J. Parvez, S. Bhatt, X. Wang, L. Gundlach, M. B. Jungfleisch, and J. Q. Xiao, “*Revisiting altermagnetism in RuO₂: a study of laser-pulse induced charge dynamics by time-domain terahertz spectroscopy*,” *npj Spintronics* **3**, 17 (2025).

[24] L. Fu, C. L. Kane, and E. J. Mele, “*Topological Insulators in Three Dimensions*,” *Phys. Rev. Lett.* **98**, 106803 (2007).

[25] W. A. Benalcazar, B. A. Bernevig, and T. L. Hughes, “*Quantized electric multipole insulators*,” *Science* **357**, 61 (2017).

[26] W. A. Benalcazar, B. A. Bernevig, and T. L. Hughes, “*Electric multipole moments, topological multipole moment pumping, and chiral hinge states in crystalline insulators*,” *Phys. Rev. B* **96**, 245115 (2017).

[27] F. Schindler, A. M. Cook, M. G. Vergniory, Z. Wang, S. S. P. Parkin, B. A. Bernevig, and T. Neupert, “*Higher-order topological insulators*,” *Science Advances*

4, eaat0346 (2018).

[28] M. Ezawa, “Higher-order topological insulators and semimetals on the breathing kagome and pyrochlore lattices,” *Phys. Rev. Lett.* **120**, 026801 (2018).

[29] S. Franca, J. van den Brink, and I. C. Fulga, “An anomalous higher-order topological insulator,” *Phys. Rev. B* **98**, 201114 (2018).

[30] D. Călugăru, V. Juričić, and B. Roy, “Higher-order topological phases: A general principle of construction,” *Phys. Rev. B* **99**, 041301 (2019).

[31] L. Trifunovic and P. W. Brouwer, “Higher-Order Bulk-Boundary Correspondence for Topological Crystalline Phases,” *Phys. Rev. X* **9**, 011012 (2019).

[32] P. Chatterjee, A. K. Ghosh, A. K. Nandy, and A. Saha, “Second-order topological superconductor via noncollinear magnetic texture,” *Phys. Rev. B* **109**, L041409 (2024).

[33] J. Langbehn, Y. Peng, L. Trifunovic, F. von Oppen, and P. W. Brouwer, “Reflection-Symmetric Second-Order Topological Insulators and Superconductors,” *Phys. Rev. Lett.* **119**, 246401 (2017).

[34] Z. Song, Z. Fang, and C. Fang, “($d - 2$)-Dimensional Edge States of Rotation Symmetry Protected Topological States,” *Phys. Rev. Lett.* **119**, 246402 (2017).

[35] E. Khalaf, “Higher-order topological insulators and superconductors protected by inversion symmetry,” *Phys. Rev. B* **97**, 205136 (2018).

[36] X. Ni, M. Weiner, A. Alù, and A. B. Khanikaev, “Observation of higher-order topological acoustic states protected by generalized chiral symmetry,” *Nature Materials* **18**, 113 (2019).

[37] M. Serra-Garcia, V. Peri, R. Süssstrunk, O. R. Bilal, T. Larsen, L. G. Villanueva, and S. D. Huber, “Observation of a phononic quadrupole topological insulator,” *Nature* **555**, 342 (2018).

[38] F. Schindler, Z. Wang, M. G. Vergniory, A. M. Cook, A. Murani, S. Sengupta, A. Y. Kasumov, R. Deblock, S. Jeon, I. Drozdov, H. Bouchiat, S. Guéron, A. Yazdani, B. A. Bernevig, and T. Neupert, “Higher-order topology in bismuth,” *Nature Physics* **14**, 918 (2018).

[39] Z. Wang, B. J. Wieder, J. Li, B. Yan, and B. A. Bernevig, “Higher-Order Topology, Monopole Nodal Lines, and the Origin of Large Fermi Arcs in Transition Metal Dichalcogenides $X\text{Te}_2$ ($X = \text{Mo, W}$),” *Phys. Rev. Lett.* **123**, 186401 (2019).

[40] R.-X. Zhang, F. Wu, and S. Das Sarma, “Möbius insulator and higher-order topology in $\text{MnBi}_{2n}\text{Te}_{3n+1}$,” *Phys. Rev. Lett.* **124**, 136407 (2020).

[41] M. Ezawa, “Detecting the Néel vector of altermagnets in heterostructures with a topological insulator and a crystalline valley-edge insulator,” *Phys. Rev. B* **109**, 245306 (2024).

[42] Y.-X. Li, Y. Liu, and C.-C. Liu, “Creation and manipulation of higher-order topological states by altermagnets,” *Phys. Rev. B* **109**, L201109 (2024).

[43] Y.-X. Li, Y. Liu, and C.-C. Liu, “Creation and manipulation of higher-order topological states by altermagnets,” *Phys. Rev. B* **109**, L201109 (2024).

[44] Y.-X. Li and C.-C. Liu, “Majorana corner modes and tunable patterns in an altermagnet heterostructure,” *Phys. Rev. B* **108**, 205410 (2023).

[45] N.-J. Yang, Z. Huang, and J.-M. Zhang, “Spin-Selective Second-Order Topological Insulators Enabling Cornertronics in Two-Dimensional Altermagnets,” *Nano Letters* **25**, 15495 (2025).

[46] S. A. A. Ghorashi, T. Li, and T. L. Hughes, “Higher-Order Weyl Semimetals,” *Phys. Rev. Lett.* **125**, 266804 (2020).

[47] H.-X. Wang, Z.-K. Lin, B. Jiang, G.-Y. Guo, and J.-H. Jiang, “Higher-Order Weyl Semimetals,” *Phys. Rev. Lett.* **125**, 146401 (2020).

[48] Z. Wang, B. J. Wieder, J. Li, B. Yan, and B. A. Bernevig, “Higher-Order Topology, Monopole Nodal Lines, and the Origin of Large Fermi Arcs in Transition Metal Dichalcogenides $X\text{Te}_2$ ($X = \text{Mo, W}$),” *Phys. Rev. Lett.* **123**, 186401 (2019).

[49] K. Wang, J.-X. Dai, L. B. Shao, S. A. Yang, and Y. X. Zhao, “Boundary Criticality of \mathcal{PT} -Invariant Topology and Second-Order Nodal-Line Semimetals,” *Phys. Rev. Lett.* **125**, 126403 (2020).

[50] H. Qiu, Y. Li, Q. Zhang, and C. Qiu, “Discovery of Higher-Order Nodal Surface Semimetals,” *Phys. Rev. Lett.* **132**, 186601 (2024).

[51] A. Pal and A. K. Ghosh, “Multi-higher-order Dirac and nodal line semimetals,” *Phys. Rev. B* **111**, 195429 (2025).

[52] A. K. Ghosh, T. Nag, and A. Saha, “Hierarchy of higher-order topological superconductors in three dimensions,” *Phys. Rev. B* **104**, 134508 (2021).

[53] H. Zhang, C.-X. Liu, X.-L. Qi, X. Dai, Z. Fang, and S.-C. Zhang, “Topological insulators in Bi_2Se_3 , Bi_2Te_3 and Sb_2Te_3 with a single Dirac cone on the surface,” *Nature Physics* **5**, 438 (2009).

[54] W. A. Benalcazar, B. A. Bernevig, and T. L. Hughes, “Quantized electric multipole insulators,” *Science* **357**, 61 (2017).

[55] See the Supplemental Material (SM) at XXXXXXXXXXXX for detailed discussions on Understanding of the Altermagnet Hamiltonian, Band structure in different topological phases, Topological Invariant, Surface theory, Details of transport calculation, Third-order TI.

[56] C.-K. Chiu, J. C. Y. Teo, A. P. Schnyder, and S. Ryu, “Classification of topological quantum matter with symmetries,” *Rev. Mod. Phys.* **88**, 035005 (2016).

[57] W. A. Benalcazar and A. Cerjan, “Chiral-Symmetric Higher-Order Topological Phases of Matter,” *Phys. Rev. Lett.* **128**, 127601 (2022).

[58] M. Subhadarshini, A. Mishra, and A. Saha, “Engineering a second-order topological superconductor hosting tunable Majorana corner modes in a magnet/d-wave superconductor hybrid platform,” *Phys. Rev. B* **112**, 125426 (2025).

[59] R. Jackiw and C. Rebbi, “Solitons with fermion number $\frac{1}{2}$,” *Phys. Rev. D* **13**, 3398 (1976).

[60] S. Datta, *Electronic Transport in Mesoscopic Systems*, Cambridge Studies in Semiconductor Physics and Microelectronic Engineering (Cambridge University Press, 1995).

[61] C. W. Groth, M. Wimmer, A. R. Akhmerov, and X. Waintal, “Kwant: a software package for quantum transport,” *New Journal of Physics* **16**, 063065 (2014).

[62] A. Pal, P. Dutta, and A. Saha, “Fermi arc mediated transport in an inversion symmetry broken Weyl semimetal nanowire and its hybrid junctions,” *Phys. Rev. B* **109**, 235419 (2024).

Supplementary Material for “Current switching behaviour mediated via hinge modes in higher order topological phase using altermagnets”

Minakshi Subhadarshini  ^{1,2,*} Amartya Pal  ^{1,2,*} and Arijit Saha  ^{1,2}

¹ Institute of Physics, Sachivalaya Marg, Bhubaneswar-751005, India

² Homi Bhabha National Institute, Training School Complex, Anushakti Nagar, Mumbai 400094, India

CONTENTS

| | |
|--|----|
| References | 6 |
| S1. Relation between altermagnets (AMs) with $d_{x^2-y^2}$ and d_{xy} symmetry | 2 |
| S2. Hamiltonian and band structure in various topological phases | 2 |
| A. Hybrid-order topological phase | 3 |
| B. SOTI phase | 4 |
| S3. Topological Invariant | 5 |
| A. Winding Number W | 5 |
| B. Quadrupolar Winding Number N_{xy} | 5 |
| S4. Surface theory | 6 |
| S5. Details of transport calculation | 8 |
| S6. Third-order TI: a possibility | 9 |
| A. Bulk Hamiltonian | 9 |
| B. Topological Invariant | 9 |
| C. Surface Hamiltonians | 10 |
| D. Hinge theory | 10 |
| E. Corner mode solution | 13 |

*MS and AP contributed equally to this work.

S1. RELATION BETWEEN ALTERMAGNETS (AMS) WITH $d_{x^2-y^2}$ AND d_{xy} SYMMETRY

In the main text, we have considered altermagnetic exchange order with $d_{x^2-y^2}$ symmetry and mentioned that $d_{x^2-y^2}$ AM is related to d_{xy} AM with a coordinate transformation. Here, we show that explicitly. In two dimensions (2D), the d_{xy} altermagnetic term can be written as [2]

$$H_{2D}(k_x, k_y) = J_{xy} k_x k_y .$$

By parameterizing the momentum as $k_x = k_F \cos \theta$ and $k_y = k_F \sin \theta$ (k_F denotes the Fermi momentum), we obtain

$$J_{xy} k_x k_y = J_{xy} k_F^2 \sin \theta \cos \theta = \frac{J_{xy} k_F^2}{2} \sin(2\theta) . \quad (\text{S1})$$

Then, we perform a rotation of the coordinate system by $\pi/4$, i.e., $\theta \rightarrow \theta' - \pi/4$. Hence,

$$\begin{aligned} \frac{J_{xy} k_F^2}{2} \sin(2\theta) &= \frac{J_{xy} k_F^2}{2} \sin(2\theta' - \pi/2) \\ &= \frac{J_{xy} k_F^2}{2} \cos(2\theta') \\ &= \frac{J_{xy} k_F^2}{2} (\cos^2 \theta' - \sin^2 \theta') \\ &= \frac{J_{xy}}{2} (k_y'^2 - k_x'^2) . \end{aligned} \quad (\text{S2})$$

Thus, rotating the frame of reference by an angle $\pi/4$, the $J_{xy} k_x k_y$ term transforms to a form proportional to $J_{xy} (k_y'^2 - k_x'^2)$.

Similarly, the other altermagnetic term transforms in the similar manner as:

$$J_{xz} k_x k_z \longrightarrow \frac{J_{xz}}{2} (k_x^2 - k_z^2) .$$

Thus, for simplicity we have only considered the AMs with $d_{x^2-y^2}$ type exchange order parameter in the main text.

S2. HAMILTONIAN AND BAND STRUCTURE IN VARIOUS TOPOLOGICAL PHASES

In the main text, we have emphasized the topological invariants, spectral properties, and transport signatures in hybrid-order and second-order topological phases considering various finite size geometries. In this section, we explicitly derive the Hamiltonians in these finite geometries namely slab, rod, and cubic geometries and also present the corresponding band structures. The latter is not shown in the main text. We begin by writing the momentum space tight-binding Hamiltonian (as mentioned in Eq. (1)-Eq. (4) of the main text) as [2, 53, 54],

$$\begin{aligned} \mathcal{H} = & 2\lambda(\sin k_x \Gamma_1 + \sin k_y \Gamma_2 + \sin k_z \Gamma_3) + [m_0 - 6t + 2t(\cos k_x + \cos k_y + \cos k_z)]\Gamma_4 \\ & + J_{xy}(\cos k_x - \cos k_y) \Gamma_5 + J_{xz}(\cos k_z - \cos k_x) \Gamma_5 , \end{aligned} \quad (\text{S3})$$

where, λ , t , and m_0 denote the spin-orbit coupling (SOC) strength, nearest-neighbour hopping amplitude, and staggered mass term with J_{xy} , J_{xz} indicate the coupling strengths of the AMs with $d_{x^2-y^2}$ and $d_{x^2-z^2}$ symmetry respectively. The Γ matrices are defined as $\Gamma_1 = \mu_x \sigma_x s_y$, $\Gamma_2 = \mu_z \sigma_0 s_0$, $\Gamma_3 = \mu_x \sigma_z s_y$, $\Gamma_4 = \mu_x \sigma_y s_y$, $\Gamma_5 = \mu_x \sigma_0 s_z$ where, μ_i , σ_i , and s_i are Pauli matrices acting on sublattice, orbital, and spin spaces.

• Slab geometry: In a three dimensional (3D) system, slab geometry corresponds to the situation when the system has finite size along any one direction, say z -direction, while the other two directions, x and y -directions, are considered to be in the momentum space so that k_x, k_y remain good quantum numbers. Usually, open boundary condition (OBC) is applied along the finite size direction. This geometry is utilized to understand the nature of the surface states present in the system. Therefore, considering slab geometry, the Hamiltonian can be written as:

$$\begin{aligned} H(k_x, k_y, z) = \sum_z c_{k_x, k_y, z}^\dagger \Big[& \left(\{m_0 - 6t + 2t(\cos k_x + \cos k_y)\} \Gamma_4 + 2\lambda(\sin k_x \Gamma_1 + \sin k_y \Gamma_2) + J_{xy}(\cos k_x - \cos k_y) \Gamma_5 \right. \\ & \left. - J_{xz} \cos k_x \Gamma_5 \right) c_{k_x, k_y, z} + \left(t\Gamma_4 - i\lambda_z \Gamma_3 + \frac{J_{xz}}{2} \right) c_{k_x, k_y, z+1} \Big] + h.c. , \end{aligned} \quad (\text{S4})$$

- **Rod geometry:** In rod geometry, the system exhibits finite size along any two directions while the other direction

is considered to be in the momentum space. The spectral properties in the rod geometry is utilized to understand the nature of the hinge localized modes which are the manifestation of second-order topological insulator (SOTI) phase. In the main text, we have used two types of rod geometry calculations considering finite size along (i) x and y directions, and (ii) x and z directions. Considering such geometry, the Hamiltonian with finite size along x and y directions can be written as,

$$H(x, y, k_z) = \sum_{x,y} c_{x,y,k_z}^\dagger \left[\left(\{m_0 - 6t + 2t(\cos k_z)\} \Gamma_4 + 2\lambda(\sin k_z) \Gamma_3 + J_{xz} \cos k_z \Gamma_5 \right) c_{x,y,k_z} \right. \\ \left. + \left(t\Gamma_4 - i\lambda_x \Gamma_1 - \frac{J_{xz}}{2} + \frac{J_{xy}}{2} \right) c_{x+1,y,k_z} + \left(t\Gamma_4 - i\lambda_y \Gamma_2 - \frac{J_{xy}}{2} \right) c_{x,y+1,k_z} \right] + h.c. , \quad (S5)$$

Similarly, Hamiltonian with finite size along x and z can be written as,

$$H(x, k_y, z) = \sum_{x,z} c_{x,k_y,z}^\dagger \left[\left(\{m_0 - 6t + 2t(\cos k_y)\} \Gamma_4 + 2\lambda(\sin k_y) \Gamma_2 - J_{xy} \cos k_y \Gamma_5 \right) c_{x,k_y,z} \right. \\ \left. + \left(t\Gamma_4 - i\lambda_x \Gamma_1 - \frac{J_{xz}}{2} + \frac{J_{xy}}{2} \right) c_{x+1,k_y,z} + \left(t\Gamma_4 - i\lambda_z \Gamma_3 + \frac{J_{xz}}{2} \Gamma_5 \right) c_{x,k_y,z+1} \right] + h.c. , \quad (S6)$$

- **Cubic geometry:** In the main text, we have used the cubic geometry to illustrate the local density of states (LDOS). In such geometry, the system has finite size along all the three directions and the corresponding Hamiltonian can be written as,

$$H = \sum_{i,j,k} c_{i,j,k}^\dagger \left[\{m_0 - 6t\} \Gamma_4 c_{i,j,k} + \left(t\Gamma_4 - i\lambda_x \Gamma_1 + \frac{J_{xy} - J_{xz}}{2} \Gamma_5 \right) c_{i+1,j,k} \right. \\ \left. + \left(t\Gamma_4 - i\lambda_y \Gamma_2 - \frac{J_{xy}}{2} \right) c_{i,j+1,k} + \left(t\Gamma_4 - i\lambda_z \Gamma_3 + \frac{J_{xz}}{2} \right) c_{i,j,k+1} \right] + h.c. , \quad (S7)$$

where,

$$c_{i,j,k} = (c_{i,j,k}^{A,\alpha,\uparrow}, c_{i,j,k}^{A,\alpha,\downarrow}, c_{i,j,k}^{A,\beta,\uparrow}, c_{i,j,k}^{A,\beta,\downarrow}, c_{i,j,k}^{B,\alpha,\uparrow}, c_{i,j,k}^{B,\alpha,\downarrow}, c_{i,j,k}^{B,\beta,\uparrow}, c_{i,j,k}^{B,\beta,\downarrow})^T .$$

Similarly, in Eq. (S4), Eq. (S5), and Eq. (S6)

$$c_{k_x, k_y, z} = (c_z^{A,\alpha,\uparrow}, c_z^{A,\alpha,\downarrow}, c_z^{A,\beta,\uparrow}, c_z^{A,\beta,\downarrow}, c_z^{B,\alpha,\uparrow}, c_z^{B,\alpha,\downarrow}, c_z^{B,\beta,\uparrow}, c_z^{B,\beta,\downarrow})_{k_x, k_y}^T ,$$

$$c_{x,y, k_z} = (c_x^{A,\alpha,\uparrow}, c_x^{A,\alpha,\downarrow}, c_x^{A,\beta,\uparrow}, c_x^{A,\beta,\downarrow}, c_y^{B,\alpha,\uparrow}, c_y^{B,\alpha,\downarrow}, c_y^{B,\beta,\uparrow}, c_y^{B,\beta,\downarrow})_{k_z}^T ,$$

$$c_{x, k_y, z} = (c_x^{A,\alpha,\uparrow}, c_x^{A,\alpha,\downarrow}, c_x^{A,\beta,\uparrow}, c_x^{A,\beta,\downarrow}, c_z^{B,\alpha,\uparrow}, c_z^{B,\alpha,\downarrow}, c_z^{B,\beta,\uparrow}, c_z^{B,\beta,\downarrow})_{k_y}^T ,$$

Here, A and B denote sublattice index and α, β are orbital index.

A. Hybrid-order topological phase

Here we use Eq. (S3) and present the surface as well as hinge spectrum by considering slab and rod geometry respectively. To construct a slab, we impose OBC along one direction while maintaining periodic boundary conditions (PBC) along the other two. In Fig. S1(a) and (e), we apply OBC along the x direction and PBC along y and z , thereby probing the yz plane. Considering the limit $k_y = 0$, we find that the surfaces along x remain gapless in case of the 3D TI. However, once the two-dimensional altermagnet term is introduced with $J_{xy} = 2t$, these surfaces become gapped. A similar behavior is observed in Fig. S1(b) and (f), where we study the y surfaces by imposing OBC along y , PBC along x and z , and fixing $k_z = 0$. In contrast, when we examine the z surfaces in Fig. S1(c) and (g) with OBC along z and PBC along x and y , we observe that the surfaces remain gapless even after turning on J_{xy} . Also in the first case, we observe that the zero-energy LDOS gives rise to modes along all surfaces as illustrated in Fig. S1(d). However, in contrast we find the surfaces are gapped for x and y appearing hinges, but the surfaces along z remains gapless as depicted in Fig. S1(h).

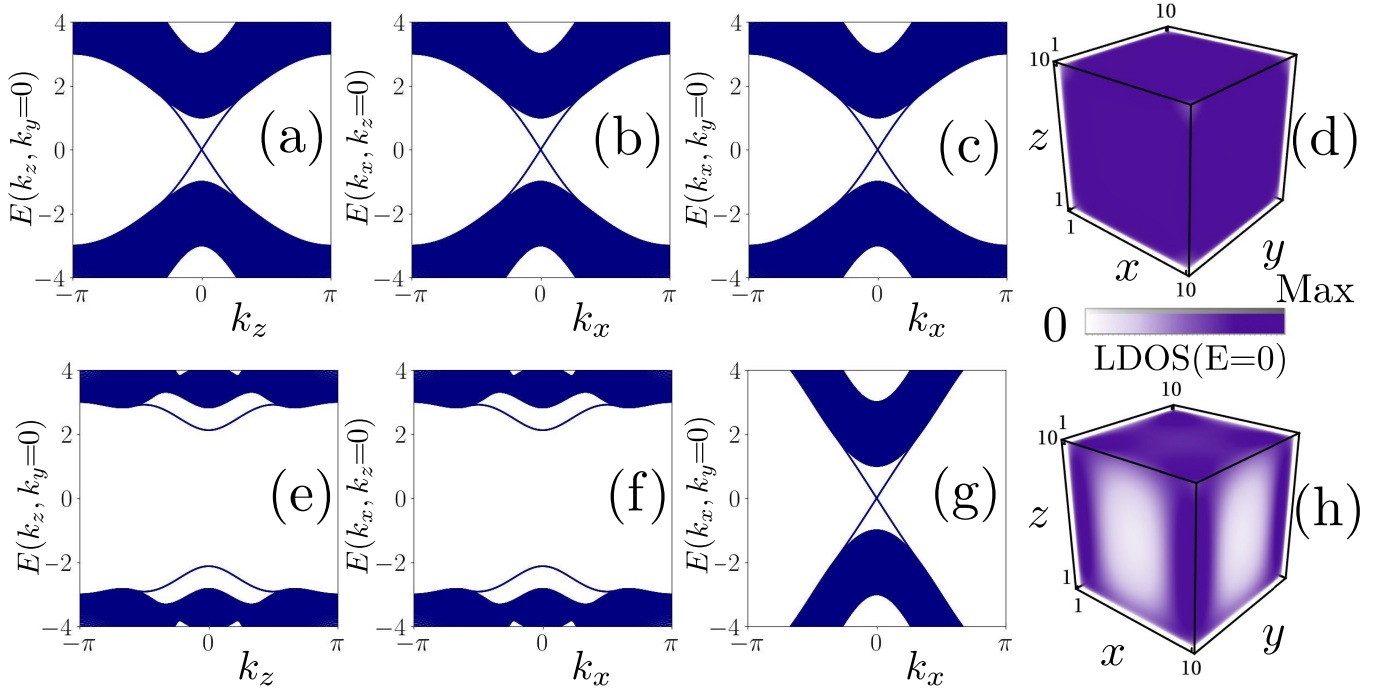


FIG. S1. 2D Surface states and corresponding LDOS for different values of J_{xy} are shown. Panels (a–c) exhibit the surface spectra for $J_{xy} = 0$, with the corresponding LDOS at $E = 0$ presented in panel (d). Panels (e–g) display the surface spectra for $J_{xy} = 2t$, and the corresponding LDOS is shown in panel (h). Other model parameters are set to be $m_0 = t$, $\lambda = t$ and $t = 1$.

B. SOTI phase

Here, we analyze the band spectrum of our system in the rod geometry considering finite J_{xz} along with J_{xy} . We explore the appearance of hinge states employing OBC along two directions and PBC along the remaining direction. In Fig. S2(a) we show that the surface normal to the z -direction becomes gapped after introducing the finite coupling J_{xz} in addition to J_{xy} . For $J_{xz} < J_{xy}$ (SOTI^(I)), the spectrum with PBC along z and OBC along x, y directions exhibits gapless 1D hinge modes propagating along z -direction (see Fig. S2(b)). On the other hand, for $J_{xz} > J_{xy}$ (SOTI^(II)), those hinge modes become gapped as shown in Fig. S2(c).

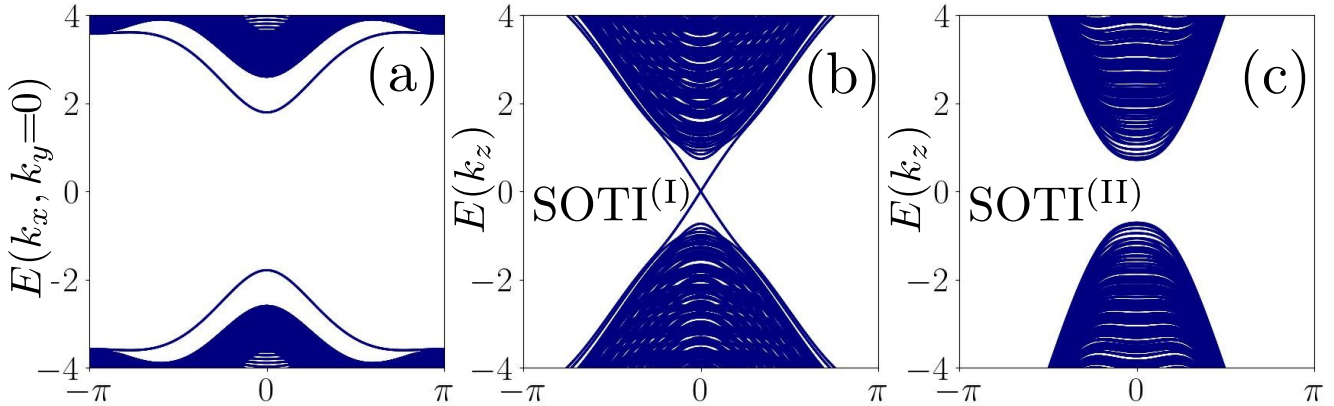


FIG. S2. We show the 2D surface state in panel (a), calculated employing OBC along the x and y directions, and with fixed momentum at $k_y = 0$. In panels (b) and (c), we display the hinge states in the SOTI phase of type I and type II, respectively. For panels (a) and (b), the model parameters are chosen as $J_{xy} = 4t$ and $J_{xz} = 2t$ respectively, while for panel (c) the same model parameters are set to $J_{xy} = 2t$ and $J_{xz} = 4t$.

S3. TOPOLOGICAL INVARIANT

We here provide the detailed formulation of the winding number (W) and the quadrupolar winding number (N).

A. Winding Number W

We start from the Hamiltonian presented in Eq. (S3) and set $k_x = k_y = 0$ and $J_{xz} = 0$. Then Eq. (S3) reduces to

$$\mathcal{H} = 2\lambda \sin k_z \Gamma_3 + [m_0 - 2t + 2t \cos k_z] \Gamma_4 . \quad (\text{S8})$$

We introduce the chiral operator as $U_s = \mu_0 \sigma_x s_0$. In this chiral basis, Eq. (S8) takes an off-diagonal form:

$$\mathcal{H} = U_c \mathcal{H} U_c^\dagger = \begin{bmatrix} 0 & h \\ h^\dagger & 0 \end{bmatrix} ,$$

where, U_c is a unitary matrix constructed from the eigenvectors of the chiral basis and h has the form $h(k) = [-2i(m_0 - 2t + 2t \cos k_z) + 4\lambda \sin k_z] \sigma_x s_y$.

The corresponding winding number is defined as [17, 56]

$$W = \frac{i}{2\pi} \int_{\text{BZ}} dk \text{Tr}[h^{-1}(k) \partial_k h(k)] . \quad (\text{S9})$$

B. Quadrupolar Winding Number N_{xy}

To compute the quadrupolar winding number in phase-1, we set $k_z = 0$ and impose PBC along x and y . The Hamiltonian preserves chiral symmetry, satisfying

$$S^\dagger H S = -H ,$$

with the chiral operator chosen as $S = \mu_y \sigma_z s_z$. In this basis, the Hamiltonian again reduces to a block off-diagonal form:

$$H = U_c H U_c^\dagger = \begin{bmatrix} 0 & h \\ h^\dagger & 0 \end{bmatrix} .$$

Here, the system is partitioned into two sublattice degrees of freedom, labeled by A and B , corresponding to the eigenvalues $+1$ and -1 of S . Thus, the eigenstates of H can be expressed as

$$|\psi_n\rangle = \begin{bmatrix} |\psi_n^A\rangle \\ |\psi_n^B\rangle \end{bmatrix} ,$$

with $|\psi_n^A\rangle$ and $|\psi_n^B\rangle$ denoting the normalized components in the respective subspaces.

Performing a singular value decomposition (SVD) of the off-diagonal block yields

$$h = U_A \Sigma U_B^\dagger ,$$

where, U_A and U_B contain the singular vectors, and Σ is diagonal with singular values.

The quadrupole operator is defined as [57]

$$Q = \exp \left(-\frac{i2\pi xy}{L_x L_y} \right) , \quad (\text{S10})$$

and the corresponding sublattice-resolved quadrupole moments are given by

$$Q_{A,B} = \sum_{R,u \in A,B} |R,u\rangle Q \langle R,u| . \quad (\text{S11})$$

Projecting these onto the SVD eigenbasis yields

$$\bar{Q}_{A,B} = U_{A,B}^\dagger Q U_{A,B} . \quad (\text{S12})$$

Finally, the **quadrupolar winding number** can be expressed as [51, 57, 58]:

$$N_{xy} = \frac{1}{2\pi i} \text{Tr} \log(\bar{Q}_{x,y}^A \bar{Q}_{x,y}^{B\dagger}) . \quad (\text{S13})$$

In phase-2, one can analogously compute:

- N_{xy} in the SOTI^(I) phase (considering OBC along $x, y, k_z = 0$), and
- N_{xz} in the SOTI^(II) phase (considering OBC along $x, z, k_y = 0$),

employing the chiral operator for N_{xy} and N_{xz} as $U = \mu_y \sigma_z s_z$ and $U = \mu_0 \sigma_0 s_x$ respectively.

S4. SURFACE THEORY

We rewrite the tight-binding Hamiltonian described in Eq. (S3) as a low energy continuum model by replacing $\sin k_i \sim k_i$ and $\cos k_i \sim (1 - k_i^2/2)$ with $i = x, y, z$. This is given by,

$$H = 2\lambda \sum_{j=1}^3 k_j \Gamma_j + \left(m_0 - t \sum_{j=1}^3 k_j^2 \right) \Gamma_4 - \frac{J_{xy}}{2} (k_x^2 - k_y^2) \Gamma_5 - \frac{J_{xz}}{2} (k_z^2 - k_x^2) \Gamma_5 . \quad (\text{S14})$$

Here, we perform the analytical calculation regarding mass inversion exhibiting surface and hinge theory. We use Eq. (S14) to derive surface and hinge Hamiltonian as we discuss later.

xy surface:-

To derive the surface Hamiltonian on the xy surface, we impose OBC along the z -direction and PBC along x and y directions. Substituting $k_z \rightarrow -i\partial_z$ and retaining only the linear terms in k_x and k_y , the Hamiltonian in Eq. (S14) separates into two parts [52, 58]:

$$\begin{aligned} H_I &= (m_0 + t\partial_z^2) \Gamma_4 - 2i\lambda\partial_z \Gamma_3 , \\ H_{II} &= 2\lambda k_x \Gamma_1 + 2\lambda k_y \Gamma_2 + \frac{J_{xz}}{2} \partial_z^2 \Gamma_5 . \end{aligned} \quad (\text{S15})$$

We first solve the eigenvalue problem $H_I |\psi\rangle = 0$ with the boundary condition $|\psi(z)\rangle \rightarrow 0$ as $z \rightarrow 0, \infty$. The solution takes the form

$$|\psi\rangle = A e^{-k_1 z} \sin(k_2 z) e^{i(k_x x + k_y y)} |\chi\rangle , \quad (\text{S16})$$

where,

$$k_1 = \frac{\lambda}{t}, \quad k_2 = \sqrt{\frac{m_0}{t} - \frac{\lambda^2}{t^2}}, \quad |A|^2 = \frac{4k_1(k_1^2 + k_2^2)}{k_2^2} . \quad (\text{S17})$$

Here, $|\chi\rangle$ is an 8-component spinor, which can be chosen as

$$\chi_1 = \begin{pmatrix} 0 \\ 0 \\ 0 \\ 0 \\ 0 \\ 1 \\ 0 \\ 1 \end{pmatrix}, \quad \chi_2 = \begin{pmatrix} 0 \\ 0 \\ 0 \\ 0 \\ 1 \\ 0 \\ 1 \\ 0 \end{pmatrix}, \quad \chi_3 = \begin{pmatrix} 0 \\ 1 \\ 0 \\ 1 \\ 0 \\ 0 \\ 0 \\ 0 \end{pmatrix}, \quad \chi_4 = \begin{pmatrix} 1 \\ 0 \\ 1 \\ 0 \\ 0 \\ 0 \\ 0 \\ 0 \end{pmatrix} . \quad (\text{S18})$$

The effective surface Hamiltonian matrix elements are obtained as

$$H_{xy,\alpha\beta}^S = \int_0^\infty dz \langle \psi_\alpha | H_{II} | \psi_\beta \rangle , \quad (\text{S19})$$

with $\alpha, \beta = 1, \dots, 8$. This yields the xy surface Hamiltonian as

$$H_{xy}^S = -2\lambda k_x \sigma_x s_y - 2\lambda k_y \sigma_z s_0 + \frac{J_{xz} m_0}{2t} \sigma_x s_z . \quad (\text{S20})$$

yz surface:-

For the yz surface, we impose OBC along x , while y and z remain periodic. Thus the Hamiltonian becomes

$$\begin{aligned} H_I &= (m_0 + t\partial_x^2)\Gamma_4 - 2i\lambda\partial_x\Gamma_1 , \\ H_{II} &= 2\lambda k_y \Gamma_2 + 2\lambda k_z \Gamma_3 + \frac{J_{xy} - J_{xz}}{2} \partial_x^2 \Gamma_5 . \end{aligned} \quad (\text{S21})$$

With the same approximation, the corresponding zero-energy mode takes the form

$$|\psi\rangle = A e^{-k_1 x} \sin(k_2 x) e^{i(k_y y + k_z z)} |\Xi\rangle , \quad (\text{S22})$$

where, the four independent spinors are

$$\Xi_1 = \begin{pmatrix} 0 \\ 0 \\ 0 \\ 0 \\ 0 \\ 0 \\ 0 \\ 1 \end{pmatrix}, \quad \Xi_2 = \begin{pmatrix} 0 \\ 0 \\ 0 \\ 0 \\ 0 \\ 0 \\ 1 \\ 0 \end{pmatrix}, \quad \Xi_3 = \begin{pmatrix} 0 \\ 0 \\ 0 \\ 1 \\ 0 \\ 0 \\ 0 \\ 0 \end{pmatrix}, \quad \Xi_4 = \begin{pmatrix} 0 \\ 0 \\ 1 \\ 0 \\ 0 \\ 0 \\ 0 \\ 0 \end{pmatrix}. \quad (\text{S23})$$

Thus the projected surface Hamiltonian can be written as

$$H_{yz}^S = -2\lambda k_y \sigma_z s_0 + 2\lambda k_z \sigma_x s_y + \frac{(J_{xy} - J_{xz}) m_0}{2t} \sigma_x s_z . \quad (\text{S24})$$

xz surface:-

In case of xz surface, we impose OBC along y direction while maintaining PBC along x and z directions. The Hamiltonian reads

$$\begin{aligned} H_I &= (m_0 + t\partial_y^2)\Gamma_4 - 2i\lambda\partial_y\Gamma_2 , \\ H_{II} &= 2\lambda k_x \Gamma_1 + 2\lambda k_z \Gamma_3 - \frac{J_{xy}}{2} \partial_y^2 \Gamma_5 . \end{aligned} \quad (\text{S25})$$

The zero-energy state is

$$|\psi\rangle = A e^{-k_1 y} \sin(k_2 y) e^{i(k_x x + k_z z)} |\xi\rangle , \quad (\text{S26})$$

with four independent spinors as

$$\xi_1 = \begin{pmatrix} -i \\ 0 \\ 0 \\ 0 \\ 0 \\ 0 \\ 0 \\ 1 \end{pmatrix}, \quad \xi_2 = \begin{pmatrix} 0 \\ i \\ 0 \\ 0 \\ 0 \\ 0 \\ 1 \\ 0 \end{pmatrix}, \quad \xi_3 = \begin{pmatrix} 0 \\ 0 \\ i \\ 0 \\ 0 \\ 1 \\ 0 \\ 0 \end{pmatrix}, \quad \xi_4 = \begin{pmatrix} 0 \\ 0 \\ 0 \\ -i \\ 1 \\ 0 \\ 0 \\ 0 \end{pmatrix}. \quad (\text{S27})$$

The corresponding surface Hamiltonian becomes

$$H_{xz}^S = -2\lambda k_x \sigma_z s_0 + 2\lambda k_z \sigma_x s_0 + \frac{J_{xy} m_0}{2t} \sigma_y s_x . \quad (\text{S28})$$

From Eq. (S24) and Eq. (S28), we observe that at $k_x = k_y = k_z = 0$ both yz and xz surfaces are gapped. Under unitary transformations

$$u_1 = \sigma_0 e^{-i\frac{\pi}{4} s_y}, \quad u_2 = \sigma_z e^{i\frac{\pi}{4} s_0},$$

with $u_2^{-1}u_1^{-1}H_{xz}u_1u_2$, the surface Hamiltonians simplify to:

$$\begin{aligned} H_{xy}^S &= \frac{J_{xz}m_0}{2t}\sigma_x s_z, \\ H_{yz}^S &= \frac{(J_{xy} - J_{xz})m_0}{2t}\sigma_x s_z, \\ H_{xz}^S &= -\frac{J_{xy}m_0}{2t}\sigma_x s_z. \end{aligned} \quad (\text{S29})$$

From Eq. (S29), it is evident that the surface Dirac masses exhibit relative sign changes. In phase-1 (HyOTP), $J_{xz} = 0$, hence the surface along xy is gapless and mass changes between xz and yz surfaces. According to Jackiew-Rebbi theorem [59], we have 1D hinge modes propagating along the z -direction.

In phase-2 (SOTI), from Eq. (S29), between the xy and xz surfaces, the mass terms always have opposite signs resulting in x -directed hinge modes. On top of that, if $J_{xz} > J_{xy}$, an additional sign change occurs between the mass terms of xy and yz surfaces, leading to hinge modes along the x and y directions (SOTI^(II)). Conversely, if $J_{xy} > J_{xz}$, the additional sign change appears between the yz and xz surfaces, giving rise to hinge modes along the x and z directions (SOTI^(I)).

S5. DETAILS OF TRANSPORT CALCULATION

In the main text, we have computed the two terminal differential conductance, dI/dV , to identify the surface states as well as hinge states in different topological phases. Here, we discuss the computational details of the transport calculation. To obtain the differential conductance, we first construct the scattering matrix, which relates the incoming propagating modes to the outgoing modes in the leads with the central system being considered as the scatterer. Incoming, outgoing states and the scattering matrix are defined as:

$$\Psi^{\text{in}} = [\psi_1^L, \psi_2^L, \dots, \psi_{N_L}^L, \psi_1^R, \psi_2^R, \dots, \psi_{N_R}^R]^T, \quad (\text{S30})$$

$$\Phi^{\text{out}} = [\phi_1^L, \phi_2^L, \dots, \phi_{N_L}^L, \phi_1^R, \phi_2^R, \dots, \phi_{N_R}^R]^T, \quad (\text{S31})$$

$$\Phi^{\text{out}} = \hat{S}\Psi^{\text{in}},$$

where, $\psi_i^{\text{L(R)}}$ is the incoming state from the left (right) lead in the i^{th} mode. Here, $N_L(N_R)$ is the number of occupied modes/channels in the left (right) lead for a given voltage bias eV . Similarly, $\phi_i^{\text{L(R)}}$ is the outgoing state into the left (right) lead in the i^{th} mode after the scattering event takes place. Here, ' T ' denotes the transpose operation. The unitary scattering matrix \hat{S} of dimension $(N_L + N_R) \times (N_L + N_R)$ reads

$$\hat{S} = \begin{bmatrix} \hat{r} & \hat{t}' \\ \hat{t} & \hat{r}' \end{bmatrix}, \quad (\text{S32})$$

where, $\hat{r}(\hat{r}')$ is a square matrix of dimension $N_L(N_R)$ and $\hat{t}(\hat{t}')$ is a matrix of dimension $N_R \times N_L(N_L \times N_R)$. Physically, $\hat{r}(\hat{r}')$ represents the reflection matrix with elements $r_{i,j}(r'_{i,j})$ being the amplitude of reflection from the j^{th} mode to the i^{th} -mode in the left (right) lead. Similarly, $\hat{t}(\hat{t}')$ denotes the transmission matrix with elements $t_{i,j}(t'_{i,j})$ denoting the amplitude of the transmission from the j^{th} mode in left (right) lead to the i^{th} mode in the right (left) lead following the unitarity condition: $r^\dagger r + t^\dagger t = \mathcal{I}$. Within this formalism, the two-terminal differential conductance at zero temperature can be obtained using the Landauer formula given by [60],

$$\frac{dI}{dV}(eV) = G_0 \text{Tr}[t^\dagger(E)t(E)]|_{E=eV}, \quad (\text{S33})$$

where $G_0 = e^2/h$ is the unit of quantum conductance. The scattering amplitudes can be calculated numerically using python package KWANT [61].

For the surface states in the hybrid order topological phase, we attach two leads at $x = 1$ and $x = L_x$ (see inset of Fig. 1(a) of the main text) and apply a voltage bias eV across the leads. Importantly, we model both the leads and the system using the Hamiltonian in the slab geometry as mentioned in Eq. (S4). The leads are attached along the x -direction which capture all the transverse modes propagating along the x -direction. However, the surface states also have propagating modes along the y -direction. To incorporate these modes, we sum over all k_y in the dI/dV calculation as,

$$\frac{dI^{(S)}}{dV}(eV) = G_0 \sum_{k_y} \text{Tr}[t_S^\dagger(E)t_S(E)]|_{E=eV} , \quad (\text{S34})$$

where, $t_S(E)$ is the scattering the matrix in the transport setup mentioned above.

Similarly, for the hinge states which propagate along the z -direction, we attach two leads at $z = 1$ and $z = L_z$, and apply a voltage bias eV across the leads. Importantly, for this case, we model the leads and the system using the Hamiltonian in the rod geometry as mentioned in Eq. (S5). Since in this case, the system carries propagating modes only along the z -direction while the modes are localized in the other directions, we use the following expression to obtain the dI/dV ,

$$\frac{dI^{(H)}}{dV}(eV) = \frac{e^2}{h} \text{Tr}[t_H^\dagger(E)t_H(E)]|_{E=eV} , \quad (\text{S35})$$

where, $t_H(E)$ denotes the scattering matrix containing all the information about the transverse modes in this geometry.

S6. THIRD-ORDER TI: A POSSIBILITY

In this section, we put forward a purely theoretical proposal for engineering third order TI (TOTI). If a unconventional magnet with d -wave magnetic order exists in the form of $d_{r^2-3z^2}$ and $r^2 = x^2 + y^2 + z^2$, then the form of the exchange term can be given as $J_2(k_x^2 + k_y^2 - 2k_z^2)$.

A. Bulk Hamiltonian

We first rewrite the tight-binding Hamiltonian (Eq. (S3)) as a low energy continuum model by replacing $\sin k_i \rightarrow k_i$ and $\cos k_i \rightarrow (1 - k_i^2/2)$ with $i = x, y, z$ as,

$$H = 2\lambda \sum_{j=1}^3 k_j \Gamma_j + \left(m_0 - t \sum_{j=1}^3 k_j^2 \right) \Gamma_4 - \frac{J_{xy}}{2} (k_x^2 - k_y^2) \Gamma_5 + \frac{J_{xz}}{2} (k_z^2 - k_x^2) \Gamma_5 + J_2(k_x^2 + k_y^2 - 2k_z^2) \Gamma_6 , \quad (\text{S36})$$

where, $\Gamma_6 = \mu_x \sigma_0 s_x$. Employing OBC in all three spatial directions, the hinge states become fully gapped (see Fig. S3(a-c)), giving rise to a TOTI phase. In this regime, the octupolar winding number is quantized at $O_{xyz} = 1$ as shown in Fig. S3(d). This signifies a single zero-energy mode bound to each corner (see Fig. S3(f)). Finite-size scaling of the topological gap, performed for lattice sizes from $8 \times 8 \times 8$ to $16 \times 16 \times 16$, exhibits the gap closing systematically with increasing system size [inset of Fig. S3(d)]. For the $16 \times 16 \times 16$ lattice, the eigenvalue spectrum (Fig. S3(e)) reveals eight zero-energy modes, consistent with the presence of one mode per corner. The corresponding zero-energy LDOS distribution confirms sharply localized corner states as depicted in Fig. S3(f).

B. Topological Invariant

To calculate the octupolar winding number (O_{xyz}), we instead use the chiral operator $U = \mu_y \sigma_0 s_0$. The corresponding octapole operator is defined as [57]

$$O = \exp \left(-\frac{i 2\pi xyz}{L_x L_y L_z} \right) . \quad (\text{S37})$$

Projecting into the sublattice sectors yields

$$\bar{O}_{A,B} = U_{A,B}^\dagger O U_{A,B} , \quad (\text{S38})$$

and the octupolar winding number follows as

$$O_{xyz} = \frac{1}{2\pi i} \text{Tr} \log(\bar{O}_{x,y,z}^A \bar{O}_{x,y,z}^{B\dagger}) . \quad (\text{S39})$$

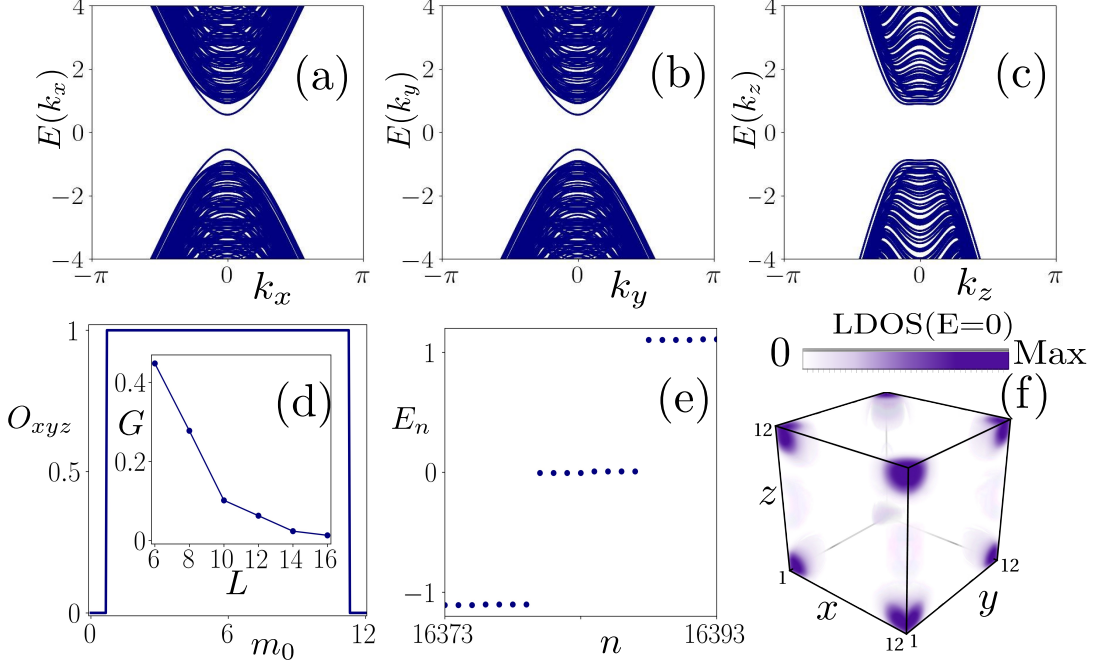


FIG. S3. Panels (a-c) display the gapped hinge spectrum. The octupolar winding number O_{xyz} is shown as a function of m_0 in panel (d). The inset shows the finite-size scaling of the energy gap at fixed $m_0 = 2t$. In panel (e), we depict the eigenvalue spectrum E_n as a function of the state index n considering $16 \times 16 \times 16$ lattice size. Panel (f) illustrates the zero-energy LDOS, revealing corner localized modes in $12 \times 12 \times 12$ system size. The model parameters are chosen as $J_{xy} = 2t$, $J_{xz} = 0$ and $J_2 = 4t$, while the remaining settings remain the same as mentioned in Fig. S2.

C. Surface Hamiltonians

To derive the surface Hamiltonian for the xy surface, we consider OBC in the z direction and PBC in x and y directions. Replacing $k_z \rightarrow -i\partial_z$ and keeping terms upto first order in k_x and k_y , we divide the Hamiltonian into two parts:

$$\begin{aligned} H_I &= (m_0 + t\partial_z^2)\Gamma_4 - 2i\lambda\partial_z\Gamma_3 , \\ H_{II} &= 2\lambda k_x\Gamma_1 + 2\lambda k_y\Gamma_2 + \frac{J_{xz}}{2}\partial_z^2\Gamma_5 + J_2\partial_z^2\Gamma_6 . \end{aligned} \quad (\text{S40})$$

Solving the Hamiltonian as described before we obtain the surface Hamiltonian as

$$H_{xy}^S = -2\lambda k_x\sigma_x s_y - 2\lambda k_y\sigma_z s_0 - \frac{J_2 m_0}{t}\sigma_x s_x + \frac{J_{xz} m_0}{2t}\sigma_x s_z , \quad (\text{S41})$$

For the yz surface, we impose OBC along x and PBC along y and z . The surface Hamiltonian becomes

$$H_{yz}^S = -2\lambda k_y\sigma_z s_0 + 2\lambda k_z\sigma_x s_y + \frac{(J_{xy} - J_{xz})m_0}{2t}\sigma_x s_z , \quad (\text{S42})$$

Similarly, for the xz surface, we impose OBC along y , while x and z have PBC. The surface Hamiltonian can be written as

$$H_{xz}^S = -2\lambda k_x\sigma_z s_0 + 2\lambda k_z\sigma_x s_0 - \frac{J_2 m_0}{2t}\sigma_y s_z + \frac{J_{xy} m_0}{2t}\sigma_y s_x . \quad (\text{S43})$$

Using the surface Hamiltonians H_{xy}^S , H_{yz}^S , H_{xz}^S , we proceed to construct the Hinge theory.

D. Hinge theory

Hinge mode of xy along y :

To obtain the hinge modes, we start from the surface Hamiltonian. Considering OBC along x and PBC along y , the Hamiltonian decomposes into:

$$\begin{aligned} H_I &= 2i\lambda\partial_x\sigma_x s_y + \frac{J_{xz}m_0}{2t}\sigma_x s_z, \\ H_{II} &= -2\lambda k_y\sigma_z s_0 - \frac{J_2m_0}{t}\sigma_x s_x. \end{aligned} \quad (\text{S44})$$

We solve $H_I|\psi\rangle = 0$ with boundary condition $|\psi\rangle \rightarrow 0$ as $x \rightarrow 0$. The solution is:

$$|\psi\rangle \sim e^{-\zeta x + ik_y y} |\chi_\alpha\rangle, \quad (\text{S45})$$

with

$$\zeta = \left\{ -\frac{J_{xz}m_0}{4\lambda t}, -\frac{J_{xz}m_0}{4\lambda t}, \frac{J_{xz}m_0}{4\lambda t}, \frac{J_{xz}m_0}{4\lambda t} \right\},$$

and

$$\chi_1 = \begin{pmatrix} 0 \\ 0 \\ 1 \\ 1 \end{pmatrix}, \quad \chi_2 = \begin{pmatrix} 1 \\ 1 \\ 0 \\ 0 \end{pmatrix}. \quad (\text{S46})$$

The hinge Hamiltonian along x is:

$$H_{xy,y}^H = 2\lambda k_y\sigma_z - \frac{J_2m_0}{t}\sigma_x. \quad (\text{S47})$$

Hinge mode of xy along x :

For hinge mode along x , we consider OBC along y and PBC along x , the Hamiltonian decomposes into:

$$\begin{aligned} H_I &= 2i\lambda\partial_y\sigma_z s_0 + \frac{J_{xz}m_0}{2t}\sigma_x s_z, \\ H_{II} &= -2\lambda k_x\sigma_x s_y - \frac{J_2m_0}{t}\sigma_x s_x. \end{aligned} \quad (\text{S48})$$

The zero-energy solution is of the form

$$|\psi\rangle \sim e^{-\zeta y + ik_x x} |\chi_\alpha\rangle, \quad (\text{S49})$$

with the same ζ as mentioned before and

$$\chi_1 = \begin{pmatrix} 0 \\ i \\ 0 \\ 1 \end{pmatrix}, \quad \chi_2 = \begin{pmatrix} -i \\ 0 \\ 1 \\ 0 \end{pmatrix}. \quad (\text{S50})$$

The hinge Hamiltonian becomes

$$H_{xy,x}^H = -2\lambda k_x\sigma_x + \frac{J_2m_0}{t}\sigma_y. \quad (\text{S51})$$

Hinge mode of xz along z :

For the xz surface and hinge modes along z , considering OBC along x and PBC along z , we decompose:

$$\begin{aligned} H_I &= 2i\lambda\partial_z\sigma_z s_0 + \frac{J_{xy}m_0}{2t}\sigma_y s_x, \\ H_{II} &= 2\lambda k_z\sigma_x s_0 - \frac{J_2m_0}{2t}\sigma_y s_z. \end{aligned} \quad (\text{S52})$$

The zero-energy solution is:

$$|\psi\rangle \sim e^{-\zeta z + ik_x z} |\chi_\alpha\rangle, \quad (\text{S53})$$

with

$$\zeta = \left\{ -\frac{J_{xy}m_0}{4\lambda t}, -\frac{J_{xy}m_0}{4\lambda t}, \frac{J_{xy}m_0}{4\lambda t}, \frac{J_{xy}m_0}{4\lambda t} \right\},$$

and

$$\chi_1 = \begin{pmatrix} -1 \\ 0 \\ 0 \\ 1 \end{pmatrix}, \quad \chi_2 = \begin{pmatrix} 0 \\ -1 \\ 1 \\ 0 \end{pmatrix}. \quad (\text{S54})$$

The hinge Hamiltonian along z can be written as

$$H_{xz,z}^H = -2\lambda k_z \sigma_x + \frac{J_2 m_0}{2t} \sigma_y. \quad (\text{S55})$$

Hinge mode of xz along x :

Employing OBC along z and PBC along x , the zero-energy solution is:

$$|\psi\rangle \sim e^{-\zeta z + ik_x x} |\chi_\alpha\rangle, \quad (\text{S56})$$

with

$$\chi_1 = \begin{pmatrix} i \\ -i \\ 0 \\ 0 \end{pmatrix}, \quad \chi_2 = \begin{pmatrix} 0 \\ 0 \\ 1 \\ 1 \end{pmatrix}. \quad (\text{S57})$$

The hinge Hamiltonian is:

$$H_{xz,x}^H = -2\lambda k_x \sigma_z + \frac{J_2 m_0}{2t} \sigma_x. \quad (\text{S58})$$

Hinge mode of yz along z :

For the yz surface, with OBC along y and PBC along z , we write:

$$\begin{aligned} H_I &= 2i\lambda \partial_z \sigma_z s_0 + \frac{J_{xy}m_0}{2t} \sigma_x s_z, \\ H_{II} &= 2\lambda k_z \sigma_x s_y + \frac{J_2 m_0}{2t} \sigma_x s_x - \frac{J_{xz}m_0}{2t} \sigma_x s_z. \end{aligned} \quad (\text{S59})$$

The solution becomes

$$|\psi\rangle \sim e^{-\zeta y + ik_z z} |\chi_\alpha\rangle, \quad (\text{S60})$$

with

$$\zeta = \left\{ -\frac{J_{xy}m_0}{4\lambda t}, -\frac{J_{xy}m_0}{4\lambda t}, \frac{J_{xy}m_0}{4\lambda t}, \frac{J_{xy}m_0}{4\lambda t} \right\},$$

and

$$\chi_1 = \begin{pmatrix} 0 \\ i \\ 0 \\ 1 \end{pmatrix}, \quad \chi_2 = \begin{pmatrix} -i \\ 0 \\ 1 \\ 0 \end{pmatrix}. \quad (\text{S61})$$

The hinge Hamiltonian can be written as

$$H_{yz,z}^H = 2\lambda k_z \sigma_x - \frac{J_2 m_0}{2t} \sigma_y. \quad (\text{S62})$$

Hinge mode of yz along y :

In this case, imposing OBC along z and PBC along y , the solution is:

$$|\psi\rangle \sim e^{-\zeta z + ik_y y} |\chi_\alpha\rangle, \quad (\text{S63})$$

with

$$\chi_1 = \begin{pmatrix} 0 \\ 0 \\ -1 \\ 1 \end{pmatrix}, \quad \chi_2 = \begin{pmatrix} -1 \\ 1 \\ 0 \\ 0 \end{pmatrix}. \quad (\text{S64})$$

The hinge Hamiltonian is:

$$H_{yz,y}^H = 2\lambda k_y \sigma_z - \frac{J_2 m_0}{2t} \sigma_x. \quad (\text{S65})$$

E. Corner mode solution

We now provide the solution for the corner modes located at $x = y = z = 0$. Solving the hinge Hamiltonian with appropriate boundary conditions and matching at $x = y = z = 0$, we obtain

$$\begin{aligned} \Phi &\sim c_1^x \phi_1 e^{-\frac{J_2 m_0 x}{2\lambda t}} + c_2^x \phi_2 e^{-\frac{J_2 m_0 x}{4\lambda t}} && : \text{along } x, \\ &\sim c_1^y \phi_2 e^{-\frac{3J_2 m_0 y}{4\lambda t}} && : \text{along } y, \\ &\sim c_1^z \phi_1 e^{-\frac{J_2 m_0 z}{2\lambda t}} && : \text{along } z, \end{aligned} \quad (\text{S66})$$

where the spinors are

$$\phi_1 = \{1, 0\}, \quad \phi_2 = \{-i, 1\}.$$

Therefore, the corner modes decay along all the directions (x, y, z) with different localization lengths depending on the parameters t, λ, m_0 and J_2 .